Geophysical Research Letters

RESEARCH LETTER
10.1029/2024GL112557

Key Points:

- The evolution of a tropical cyclone's outer rainband over the open ocean is divided into three stages: pre-mature, mature and post-mature
- The mature stage features active ice-phase and warm rain processes, while the pre-mature and post-mature stages display ice-phase dominance
- In the mature stage, most convective cells contain high concentrations of small raindrops, with a few exhibiting extremely large raindrops

Supporting Information:

Supporting Information may be found in the online version of this article.

Correspondence to:

Y. Du and B. Han,
duyu7@mail.sysu.edu.cn;
bh3917@princeton.edu

Citation:

Yang, S., Du, Y., Han, B., Wu, C., & Kong, H. (2025). Microphysical characteristics of tropical cyclone Choiwan (2021) outer rainbands derived from polarimetric radar observations on a research vessel. *Geophysical Research Letters*, *52*, e2024GL112557. https://doi.org/10.1029/2024GL112557

Received 14 SEP 2024
Accepted 9 FEB 2025

Microphysical Characteristics of Tropical Cyclone Choiwan (2021) Outer Rainbands Derived From Polarimetric Radar Observations on a Research Vessel

Shimin Yang[1,2,3], Yu Du[1,2,3], Bin Han[4], Chong Wu[5], and Hoiio Kong[6]

[1]School of Atmospheric Sciences, Sun Yat-sen University, and Southern Marine Science and Engineering Guangdong Laboratory (Zhuhai), Zhuhai, China, [2]Guangdong Province Key Laboratory for Climate Change and Natural Disaster Studies, Sun Yat-sen University, Zhuhai, China, [3]Key Laboratory of Tropical Atmosphere-Ocean System, Sun Yat-sen University, Ministry of Education, Zhuhai, China, [4]Program in Atmospheric and Oceanic Sciences, Princeton University, Princeton, NJ, USA, [5]State Key Lab of Severe Weather, Chinese Academy of Meteorological Sciences, Beijing, China, [6]Faculty of Data Science, City University of Macau, Macau, China

Abstract Microphysical characteristics of tropical cyclones (TCs) over the open ocean remain elusive due to observation constraints. In this study, dual-polarization observations derived from a ship-borne C-band polarimetric radar are utilized to investigate the microphysical characteristics of an outer rainband associated with TC Choiwan during its evolution over the South China Sea from 0500 to 1300 UTC on 3 June 2021. Based on TC and convection intensity, the eight-hour period is categorized into three stages with distinct microphysical features: pre-mature, mature and post-mature. During the mature stage, both ice-phase and warm rain processes are active, resulting in a distribution pattern where most convective cells (CCs) contain high concentrations of small raindrops with a few exhibiting extremely large raindrops, and making raindrop size distributions (DSDs) fall between "continental-like" and "maritime-like". In the pre-mature and post-mature stages, ice-phase processes predominantly govern the growth of raindrops, with CCs displaying "continental-like" DSD characteristics.

Plain Language Summary Tropical cyclone (TC) outer rainbands are important convective systems located on the periphery of a TC, often causing severe weather events like heavy rainfall. Understanding their microphysical characteristics is essential for comprehending and predicting these events. However, studying the microphysics of outer rainbands is particularly challenging when a TC is located over the open ocean due to limited observation opportunities. In this study, a C-band polarimetric radar on the research vessel *Tan Kah Kee* observed an outer rainband of TC Choiwan (2021) in the South China Sea. This fortunate opportunity allowed for a detailed examination of the rainband's microphysical structures. The study found that different microphysical features emerge during the various stages of the TC's evolution. The mature stage manifests both active ice-phase and warm rain processes, with more clear distinction between small and large raindrops, while the pre-mature and post-mature stages display ice-phase dominance. These findings deepen our understanding of the microphysical complexities in TC Choiwan's outer rainbands and provide valuable insights into their evolution across different stages of convection intensity.

1. Introduction

Tropical cyclone (TC) outer rainbands, situated at a radial distance of more than 150 km from the TC centers (Skwira et al., 2005; Willoughby et al., 1984), are crucial convective systems that significantly influence the evolution of TCs and surface precipitation (D. Wu et al., 2018). Understanding the microphysical processes within TC outer rainbands is essential. It contributes to optimizing microphysical parameterization schemes in numerical models, yielding valuable scientific advancements and social benefits.

Since the introduction of dual-polarization observations by Seliga and Bringi (1976, 1978), polarimetric radars have become instrumental in investigating microphysical processes within convective systems (Bringi et al., 2003; Wang et al., 2019). Compared to conventional weather radars, polarimetric radars provide more detailed polarimetric measurements, including horizontal radar reflectivity (Z_H) revealing convection intensity, differential reflectivity (Z_{DR}) indicating drop sizes, special differential phase (K_{DP}) reflecting raindrop concentrations and correlation coefficient (ρ_{hv}) related to drop uniformity. These polarimetric observations can be used to retrieve

additional microphysical parameters such as raindrop size distributions (DSDs), including mass-weighted mean diameter (D_m) and normalized intercept parameter (N_w) (Bringi et al., 2002, 2003; Gorgucci et al., 2002), as well as liquid water content (LWC) (e.g., Carey & Rutledge, 2000; Chang et al., 2015; Cifelli et al., 2002; Han et al., 2021; Li et al., 2020). Moreover, the method of microphysical fingerprints has been proposed and applied to visualize precipitation microphysical processes using polarimetric radar observations (Kumjian et al., 2022). This approach is particularly effective in identifying dominant warm rain processes, such as coalescence, evaporation, size sorting and breakup, by examining vertical changes in radar variables Z_H and Z_{DR} (Kumjian & Prat, 2014).

DSDs are fundamental microphysical characteristics of precipitation, primarily reflecting the mean size of raindrops through D_m and their number concentration through N_w. According to DSDs, convective precipitation systems can generally be classified into two types: continental-like (higher raindrop diameter and lower raindrop concentration) and maritime-like (lower raindrop diameter and higher raindrop concentration), as suggested by Bringi et al. (2003). For TCs, DSDs often feature high concentrations of small and/or mid-size drops (DeHart & Bell, 2020; Feng et al., 2023; Tokay et al., 2008; Zheng et al., 2021). Additionally, DSDs exhibit spatial and temporal variabilities (Bringi et al., 2003), and are influenced by rainfall types (Nzeukou et al., 2004), climatic regions (Tang et al., 2014), monsoon seasons (Radhakrishna & Narayana Rao, 2010), and even the measuring principles, including the types of disdrometers used (Radhakrishna, 2022). For instance, Chang et al. (2009) employed a 2-D video disdrometer (2DVD) and found that typhoons making landfall in Taiwan exhibit maritime-like DSDs over the ocean, transitioning to a mix of maritime-like and continental-like characteristics after landfall. Wen et al. (2018) utilized three 2DVDs and observed that typhoon rainfall in continental China shows more maritime-like characteristics than in Taiwan. Feng et al. (2020) used 2DVD data and revealed that DSDs in the outer rainband of a typhoon after landfall are characterized by high concentrations of small drops (<1 mm) and some extremely large drops (>5 mm). Janapati et al. (2017) used a PARSIVEL disdrometer and suggested that post-landfall precipitation exhibits higher D_m values compared to pre-landfall conditions, which is somewhat consistent with the conclusion of Chang et al. (2009). Furthermore, interactions between the TC, surrounding environment, and underlying surface can result in distinct microphysical processes, leading to different DSDs.

In recent years, the upgrade of multiple weather radars along the coasts of China to polarimetric ones has significantly advanced research on rain microphysics of landfalling TCs. Wang et al. (2016) discovered that warm rain processes dominate within the inner rainband of landfalling typhoon in Eastern China, particularly through cloud water accretion by raindrops. Wen et al. (2018) also emphasized the predominance of warm rain processes during typhoon rainfall in China. Contrastingly, D. Wu et al. (2018) proposed that ice-phase processes dominate in a typhoon outer rainband over land and highlighted the significance of riming. Additionally, Z. Wu et al. (2021) highlighted the importance of melting in the outer rainband. Feng et al. (2023) further noted that warm rain processes produce more liquid water before typhoon landfalling, while ice-phase processes become predominant after landfall. Microphysical processes within TCs in other ocean basins have also been investigated. In the southern peninsula of India, Subrahmanyam and Baby (2020) showed that the outer rainbands of TC Ockhi (2017) are characterized by the coexistence of large ice particles and lofted supercooled water. In the United States, Hu et al. (2020) found that the inner eyewalls of two landfalling hurricanes are dominated by warm rain processes, while the outer rainbands exhibit intense mixed-phase processes.

Previous studies on the microphysical characteristics of TC outer rainbands have primarily focused on landfalling typhoons, utilizing disdrometers and polarimetric radars installed in coastal areas. However, due to limited maritime observations, there is a noticeable gap in research on microphysical features of TCs during their evolution over the open ocean. During the KK2101 investigation voyage in the South China Sea aboard the research vessel *Tan Kah Kee*, an outer rainband of TC Choiwan was observed using a ship-borne C-band Doppler radar. This provided a valuable opportunity to investigate the microphysical characteristics of the TC's outer rainband over the sea.

2. Data and Methodology

2.1. Data

The data utilized in the present study are as follows: (a) The best track and minimum central pressure of TC Choiwan from the China Meteorological Administrator (CMA)'s TC database with a 6-h temporal resolution (Lu et al., 2021; Ying et al., 2014). (b) Environmental conditions from the European Center for Medium-Range Weather Forecasts (ECMWF) hourly reanalysis data (ERA5), featuring a horizontal resolution of

0.25° × 0.25°. (c) Soundings launched from the research vessel with a time interval of 6 h. (d) Rainfall observations derived from an automatic weather station (AWS) boarded on the research vessel. (e) Measurements obtained from a C-band Doppler radar mounted on the research vessel, including spectrum width and four basic polarimetric variables (i.e., Z_H, Z_{DR}, K_{DP}, ρ_{hv}). (f) Two products—composite radar reflectivity and hydrometeor classification results—derived from polarimetric radar variables.

All the polarimetric radar variables were interpolated into a Cartesian coordinate system after quality control, with a 150-m horizontal resolution and a vertical resolution of 0.5 km spanning from 0 to 15 km altitude. A brief overview of the basic parameters of the ship-borne C-band Dopplor radar, the quality control methods (Boodoo et al., 2010; Li et al., 2014; Testud et al., 2000) and a validation of the radar data (Chen et al., 2017; Gou et al., 2018; Kou et al., 2018) is provided in Texts S1, S2, and Figure S1 in Supporting Information S1. Composite radar reflectivity represents the maximum Z_H value in a vertical column. Hydrometeor classification results, including light and moderate rain (RA), heavy rain (HR), dry snow (DS), wet snow (WS), mixture of rain and hail (RH), ice crystal (CR), graupel (GR), and big drops (BD), are identified using a modified fuzzy logic-based hydrometeor classification algorithm (HCA) (C. Wu et al., 2018). Originally designed for S-band radars, the algorithm has been successfully adapted to use with operational C-band weather radars in China.

2.2. The Identification of Convective Cells

Following the convective cell (CC) identification method outlined by Wang et al. (2019), we define a CC as a vertical column exhibiting at least 10 layers of valid data and containing at least 5 layers with Z_H exceeding 35 dBZ.

2.3. The Estimation of Liquid Water Content

Golestani et al. (1989) introduced the concept of difference reflectivity (Z_{DP}; dB), a metric that is similar in form to Z_{DR} but differs in its interpretation and applications. While Z_{DR} serves as a fundamental polarimetric variable for characterizing drop sizes, Z_{DP} is specifically used to differentiate radar reflectivity produced by rain and ice for mixed-phase precipitation, and is calculated as:

$$Z_{DP} = 10 \log (Z_h - Z_v)$$

where Z_h and Z_v denote the horizontal and vertical radar reflectivity respectively in the units of $mm^6\ mm^{-3}$. Due to the lack of a Z_{RAIN}–Z_{DP} relationship applicable to both TC environments over the open ocean and the C-band radar observations, we adopt the Z_{RAIN}–Z_{DP} relationship established by Li et al. (2020) based on 2-year disdrometer observations in Guangdong Province (near the South China Sea):

$$Z_{RAIN} = 0.0044 Z_{DP}^2 + 0.58054 Z_{DP} + 16.591$$

According to previous studies (e.g., Chang et al., 2015; Cifelli et al., 2002; Han et al., 2021; Li et al., 2020), LWC can be calculated as:

$$LWC = 3.44 \times 10^{-3} (Z_{rain})^{4/7}$$

where Z_{rain} represents the linear form of Z_{RAIN} in the unit of $mm^6\ mm^{-3}$.

2.4. Retrieval of Raindrop Size Distributions

DSDs can be derived from polarimetric measurements using the constrained-gamma (C-G) model proposed by Zhang et al. (2001), expressed as follows:

$$N(D) = N_0 D^{\mu} \exp(-\Lambda D)$$

where D (mm) is the particle diameter, $N(D)$ ($mm^{-1}\ m^{-3}$) is the raindrop concentration of D, N_0 ($mm^{-1}\ m^{-3}$) is the intercept parameter, μ is the shape parameter, and Λ (mm^{-1}) is the slope parameter. Notably, not all three parameters (N_0, μ and Λ) are independent of each other (Haddad et al., 1996; Testud et al., 2001; Ulbrich, 1983),

with a significant correlation between μ and Λ (Zhang et al., 2001, 2003). The μ–Λ relationship can be determined based on disdrometer observations, simplifying the C–G model from three parameters to two (Han et al., 2021). Liu et al. (2018) established the Λ–Z_{DR} relationship and μ–Λ relationship using 2DVD data in Guangdong Province. These relationships are adopted in the present study as:

$$\Lambda = 2.111 \times Z_{DR}^{-1.044}$$

$$\Lambda = 0.0241\mu^2 + 0.867\mu + 2.453$$

Since there is a lack of alternative Λ–Z_{DR} relationships, and considering the proximity of the South China Sea to Guangdong Province, it is reasonable to use these relationships to derive D_m and $N_{w,}$ despite the existing uncertainties, as follows:

$$D_m = \frac{4+\mu}{\Lambda}$$

$$N_w = \frac{4^4}{\pi\rho_w}\left(\frac{10^3 \mathrm{LWC}}{D_m^4}\right)$$

where ρ_w is the density of water (1 g cm^{-3}).

3. Case Overview

3.1. TC Evolution

Choiwan initially formed east of the Philippines and experienced two instances of peak intensity (minimum central pressure descended to 995 hPa) during its lifespan (Figure 1a). The first peak occurred before its landfall in the Philippines, and subsequently its intensity decreased. Upon traversing the Philippines, Choiwan entered the South China Sea, where it reinvigorated and reached its maximum intensity for the second time from 0600 to 1800 UTC on 3 June 2021. Between 0500 and 1300 UTC on June 3, during continuous observation by the research vessel, a discernible trend of TC intensity evolution was observed, as indicated by the minimum mean sea level pressure (MSLP) near the TC center (Figure 1b). The TC intensified from 0500 to 0800 UTC, peaked between 0800 and 0900 UTC, and subsequently weakened from 0900 to 1300 UTC.

3.2. Environmental Conditions

At 0504 UTC on June 3, during a period of increasing TC intensity, the convective available potential energy (CAPE) calculated from the sounding launched from the research vessel was 1367 J kg^{-1}, indicating favorable conditions for convection growth (Figure S2 in Supporting Information S1). Additionally, the freezing level was observed at 5050 m height, and the lifting condensation level (LCL) was at 605 m altitude. By 1104 UTC on the same day, as the TC intensity decreased, CAPE decreased to 1179 J kg^{-1}, indicating reduced potential energy available for convection and likely suggesting less favorable conditions for strong convection. Simultaneously, the freezing level ascended to 5170 m height, and the LCL descended to 520 m height.

4. Microphysical Characteristics of the Outer Rainband CCs

4.1. Temporal Evolution

The temporal evolution of horizontal distributions of the composite radar reflectivity is shown in Figure 1c. Notably, large values (>35 dBZ) of the reflectivity were observed within the maximum detection range of the ship-borne radar and approximately 150–200 km from the TC center, indicating the presence of an outer rainband. The horizontal areal extension of the outer rainband exhibited a pattern of expansion followed by contraction, concomitant with the fluctuation in convection intensity.

Figure 1d illustrates the time-height distributions of Z_H, Z_{DR} and K_{DP} averaged over the identified CCs from 0508 to 1300 UTC on 3 June 2021. This eight-hour period is divided into three stages: pre-mature (~0508–0738 UTC), mature (~0744–0946 UTC), and post-mature (~0952–1300 UTC). These stages are primarily determined by

10.1029/2024GL112557

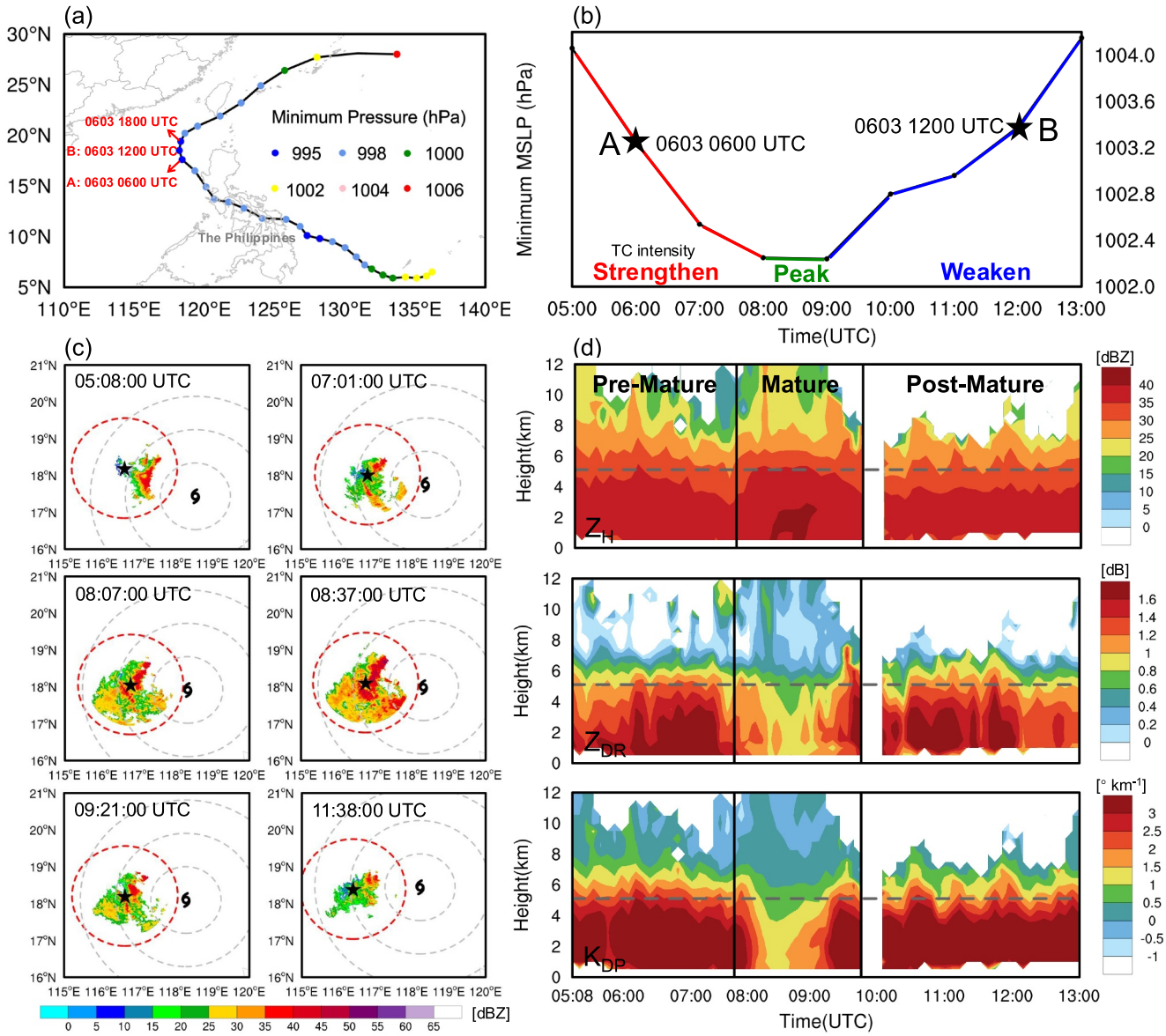

Figure 1. (a) The best track of Choiwan from CMA's TC database with a 6-h temporal resolution from 0000 UTC on 29 May to 0000 UTC on 6 June 2021. Color dots indicate the minimum central pressure (hPa). (b) Hourly temporal evolution of the minimum MSLP (hPa) near the TC center from ERA5 reanalysis data from 0500 to 1300 UTC on 3 June 2021. Red, green and blue lines indicate the strengthening, peaking and weakening of the TC intensity, respectively. (c) Horizontal distributions of composite radar reflectivity (dBZ) at 0508, 0701, 0807, 0837, 0921 and 1138 UTC on 3 June 2021, respectively. TC symbols indicate the TC centers and black stars indicate the radar locations. Gray dashed circles denote the radial distance of 100, 200, and 300 km from the TC centers respectively. Red dashed circles denote the radial distance of 150 km from the radar locations. (d) Time-height distributions of Z_H (dBZ), Z_{DR} (dB), and K_{DP} (° km^{-1}) averaged over the identified CCs at each observational time. Gray dashed lines indicate the height of freezing level.

changes observed in the time-height distributions, with additional consideration given to the temporal evolution of the minimum MSLP (Figure 1b) and the composite radar reflectivity (Figure 1c). During the mature stage, convection reached its peak intensity and depth, manifested by the tallest echo-top height of 40 dBZ, and the largest average Z_H at lower levels (from 3 to 1 km altitude). However, average Z_{DR} and K_{DP} values near and below the freezing level were significantly smaller during the mature stage compared to the pre-mature and post-mature stages. This phenomenon can be partially explained by horizontal distributions of Z_H, Z_{DR} and K_{DP}, as displayed in Text S3 and Figure S3 in Supporting Information S1.

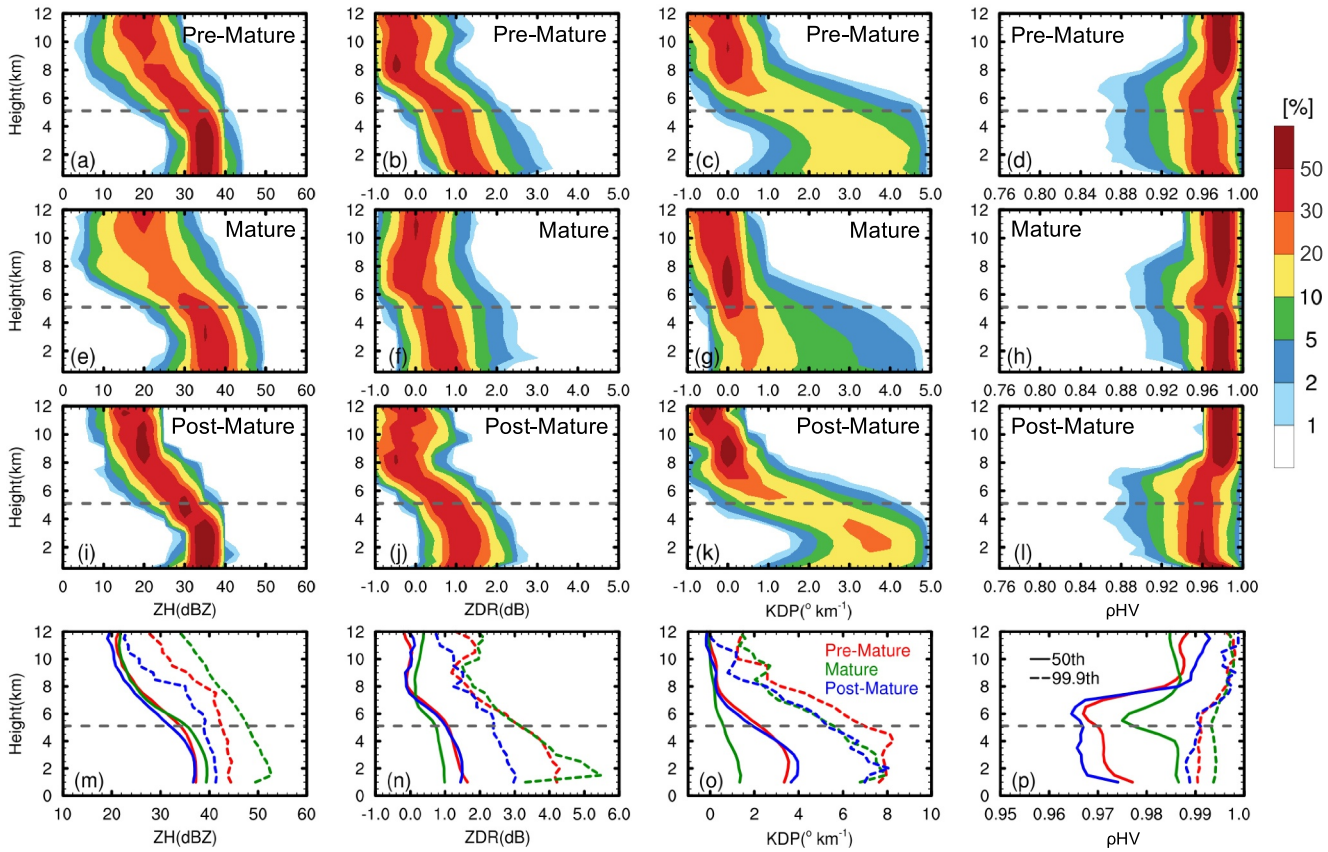

Figure 2. The CFADs (%) of (a) Z_H, (b) Z_{DR}, (c) K_{DP} and (d) ρ_{hv} for identified CCs during the pre-mature stage. Panels (e)–(h), (i)–(l) are the same as (a)–(d) but for identified CCs during the mature and post-mature stages, respectively. Panels (m)–(p) show the 50th (solid lines) and 99.9th (dashed lines) percentile profiles of (m) Z_H, (n) Z_{DR}, (o) K_{DP} and (p) ρ_{hv} for identified CCs at the pre-mature (red lines), mature (green lines) and post-mature (blue lines) stages. Gray dashed lines indicate the height of freezing level.

4.2. Polarimetric Radar Variables

Figure 2 presents contoured frequency by altitude diagrams (CFADs) and percentile profiles of polarimetric radar variables. Across all stages, the majority of Z_H distributions (with frequencies exceeding 10%) are concentrated between 30 and 40 dBZ below the freezing level (Figures 2a, 2e, and 2i). A substantial Z_H distribution within the 40–50 dBZ range along with the largest percentile profiles of Z_H at the mature stage, indicate the high intensity during this stage.

Throughout all three stages, Z_{DR} values are generally less than 2 dB (Figures 2b, 2f, and 2j), indicating that the outer rainband CCs are primarily composed of small and/or mid-size drops. During the pre-mature stage, Z_H, Z_{DR} and K_{DP} values exhibit a rapid increase near the freezing level (Figures 2a–2c), indicating active ice-phase processes and raindrop growth due to the melting of ice particles. Notably, the 50th percentile values of Z_{DR} and K_{DP} during the post-mature stage are comparable to those in the pre-mature stage (Figures 2n and 2o), which might be attributed to the continued dominance of ice-phase processes. However, key differences exist between the two stages. Generally, Z_{DR} and K_{DP} values near the freezing level are slightly larger during the pre-mature stage than those in the post-mature stage (Figure S4 in Supporting Information S1), indicating relatively stronger ice-phase processes during the pre-mature stage. Moreover, the increase in Z_{DR} and K_{DP} values at approximately 3 km height during the post-mature stage likely reflects a dominant coalescence process during this stage (Figure S5c in Supporting Information S1, Kumjian et al., 2022), as observed in decaying-phase CCs under a cyclonic environment by Kumar et al. (2024). This is also partially supported by a relatively lower LCL (Figure S2 in Supporting Information S1), which provides a deeper layer below the freezing level where the collision-

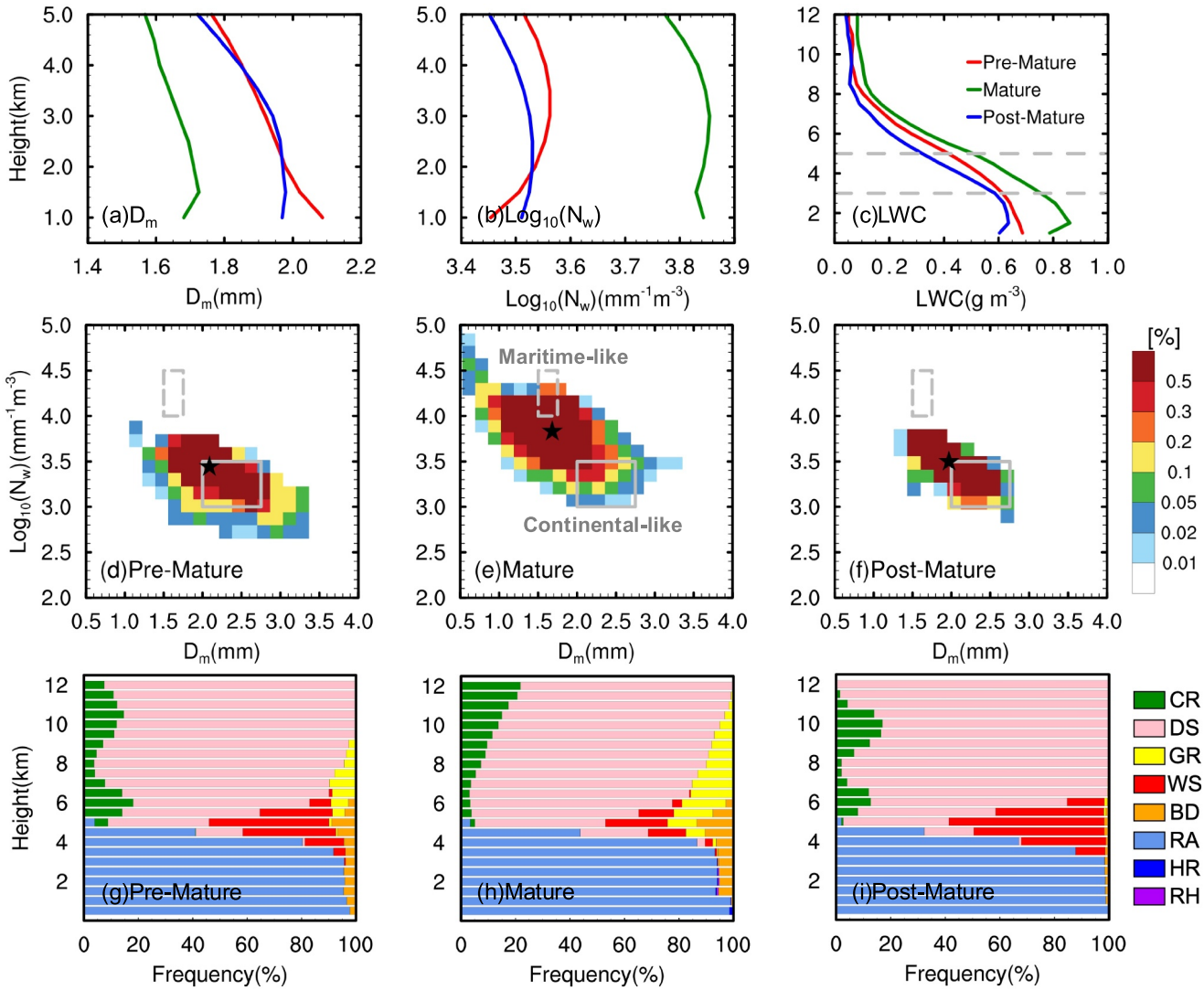

Figure 3. Mean profiles of the retrieved (a) D_m (mm), (b) $\log_{10}(N_w)$ (mm^{-1} m^{-3}) and (c) LWC (g m^{-3}) averaged over identified CCs at the pre-mature (red lines), mature (green lines) and post-mature (blue lines) stages, respectively. The gray dashed lines in (c) indicate 5 and 3 km height from up to down, respectively. Panels (d)–(f) show the joint PDFs (%) of D_m and $\log_{10}(N_w)$ at 1 km altitude for identified CCs at the (d) pre-mature, (e) mature and (f) post-mature stages. The gray dashed rectangles represent the maritime-like convective clusters, while solid ones represent the continental-like convective clusters in D_m–$\log_{10}(N_w)$ space from Bringi et al. (2003). The black stars denote the locations of mean values of D_m and $\log_{10}(N_w)$. Panels (g)–(i) show the stacked frequency (%) by altitude diagrams of each identified hydrometeor at the (g) pre-mature, (h) mature, and (i) post-mature stages.

coalescence process can occur more effectively. As the collision-coalescence process is a key component of warm rain processes, this might suggest a more efficient warm rain process during the post-mature stage.

During the mature stage, the majority of Z_{DR} and K_{DP} values near and below the freezing level are remarkably smaller compared to the other two stages (Figures 2n and 2o). The reduced values near the freezing level may result from strong riming process, as suggested by the high concentration of graupels shown in Figure 3h. This likely cause ice particles to become more rounded (Zhang et al., 2021), resulting decreases in both Z_{DR} values (Li et al., 2018) and K_{DP} values (Kumjian et al., 2022; Zheng et al., 2021). Below the freezing level, the small Z_{DR} values might indicate the presence of small raindrops, rounded ice particles, or potentially large rounded raindrops shaped by strong turbulences (Zheng et al., 2024). However, the relatively high ρ_{hv} values (Figures 2h and 2p) suggest uniformity among hydrometeor types, making a mixture of raindrops and ice particles less likely. Moreover, the lower mean spectrum width values during the mature stage, compared to the other two stages (Figure S6 in Supporting Information S1), imply that strong turbulence is unlikely to play a significant role in

lower Z_{DR}. Therefore, it is more likely that high concentrations of small raindrops dominate at lower levels during the mature stage. This also partially explains the small K_{DP} values below the freezing level (Figures 2g and 2o), as K_{DP} is relatively insensitive to spherical particles like small raindrops (Kumjian et al., 2022).

In contrast, the 99.9th percentile Z_{DR} values during the mature stage increase significantly from nearly 2 dB at 7 km height to more than 4 dB at 3 km height, indicating the growth of large raindrops driven by the melting of ice particles. Z_{DR} values also exhibit a significant increase near 2 km height, which is likely related to strong coalescence process (Figure S5b in Supporting Information S1). The remarkable increase in Z_{DR} values from 1 dB at the 50th percentile to over 5 dB at the 99.9th percentile at lower levels (Figure 2n and other percentiles shown in Figure S7 in Supporting Information S1) indicates that there are not only high concentrations of small raindrops but also a small number of exceptionally large drops during this stage. Since the statistics are based on samples of CCs, the high concentration of ρ_{hv} values around 0.98 (Figure 2h) suggests that, for most CCs, the coexistence of small and extremely large raindrops within a single CC is unlikely, as this would reduce the overall ρ_{hv} values. Therefore, the mature stage features a distribution pattern where most CCs predominantly contain small raindrops, while only a few CCs contain extremely large raindrops. Despite potential uncertainties due to overcorrection (Text S1 in Supporting Information S1), this phenomenon may be attributed to the size sorting process, leading to smaller raindrops (lower Z_{DR} values) concentrated near the convective system center and larger raindrops (higher Z_{DR} values) distributed toward the periphery (Figure S3e in Supporting Information S1).

4.3. Raindrop Size Distributions

The mean profiles of the retrieved D_m and $\log_{10}(N_w)$ are shown in Figures 3a and 3b, while the joint probability distribution functions (PDFs) of D_m and $\log_{10}(N_w)$ at 1 km altitude are depicted in Figures 3d–3f. During the pre-mature and post-mature stages, the mean D_m values of 2.09 and 1.97 mm, and $\log_{10}(N_w)$ values of 3.45 and 3.51 mm^{-1} m^{-3}, respectively, fall inside or near the continental-like clusters (Figures 3d and 3f). This indicates that the convective precipitation at these two stages shares continental-like characteristics with relatively higher diameters and lower number concentrations (Figures 3a and 3b), and suggests that the raindrop growth during these two stages is primarily driven by the melting of ice particles, as discussed in Section 4.2. During the mature stage, most of the D_m–$\log_{10}(N_w)$ pairs are located between the continental-like and maritime-like clusters, with mean $D_m = 1.68$ mm and mean $\log_{10}(N_w) = 3.84$ $mm^{-1}m^{-3}$ (Figure 3e). This suggests the smaller diameters and higher number concentrations of raindrops during the mature stage compared to the other two stages. This is likely driven by vigorous condensation of water vapor, fueled by intense sea surface evaporation and concurrently nocturnal cooling (Figure S8 in Supporting Information S1). Furthermore, the probable generation of large quantities of sea spray through wave breaking under TC conditions (Ma et al., 2020; Wang et al., 2001; Xu et al., 2023) could increase the number concentration of small droplets (Okachi et al., 2020).

4.4. Hydrometeor

We further show the stacked frequency by altitude diagrams of each identified hydrometeor for the three stages (Figures 3g–3i). During the pre-mature and mature stages, the presence of graupels above the freezing level and big drops near and below the freezing level indicate the active ice-phase processes during these two stages. Moreover, during the mature stage, the ice-phase processes, particularly riming and melting, are more efficient, characterized by the higher concentrations of graupels and big drops compared to the pre-mature stage. During the post-mature stage, the presence of graupel and big drops is minimal. Instead, there is a higher prevalence of wet snow below the freezing level that does not fully melt, suggesting relatively less active ice-phase processes compared to the preceding stages (Figure 3i). Furthermore, between 5 and 3 km height, where warm rain processes are most active, LWC increases rapidly during the post-mature stage, reaching values comparable to those observed during the pre-mature stage at around 3 km height (Figure 3c). These results indicate that ice-phase processes are relatively more active than warm rain processes during the pre-mature stage, while warm rain processes play a significant role in raindrop growth at lower levels during the post-mature stage. Both ice-phase and warm rain processes demonstrate efficiency during the mature stage.

5. Summary and Discussion

Between 0500 and 1300 UTC on 3 June 2021, Choiwan reached its second peak intensity over the South China Sea after passing through the Philippines. During this period, an outer rainband of Choiwan was continuously

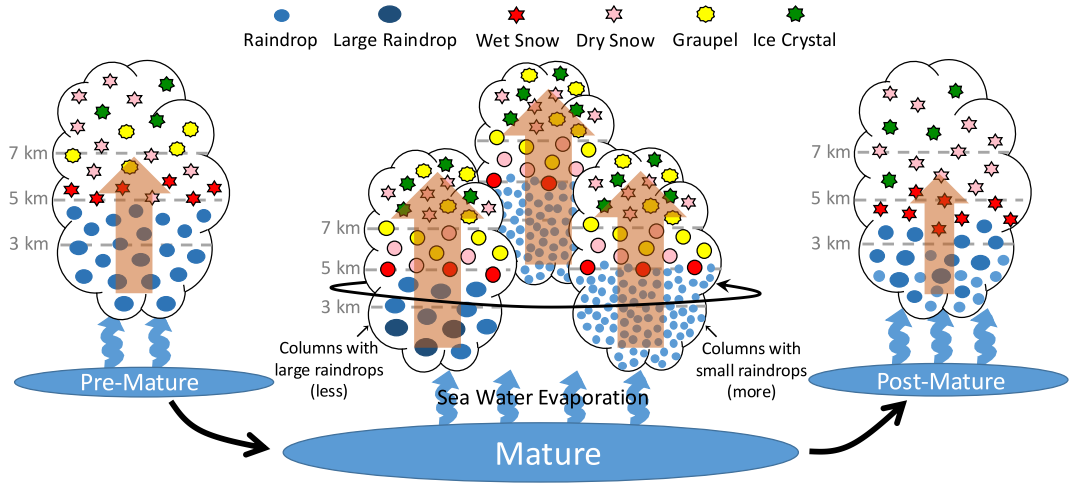

Figure 4. Schematic diagram depicting the microphysical characteristic disparities among CCs during the pre-mature, mature and post-mature stages. During the pre-mature stage, ice-phase processes are active with graupels above the freezing level and large raindrops grown by melting below the freezing level. During the mature stage, both ice-phase and warm rain processes are active. Near the freezing level, ice particles might become more rounded due to strong riming process. Below the freezing level, it exhibits a distribution pattern where a majority of CCs near the convective system center containing high concentrations of small raindrops and a few peripheral CCs featuring extremely large drops. During the post-mature stage, ice phase processes are relatively weak with minimal graupel and a higher prevalence of wet snow below the freezing level. Besides, coalescence contributes to the growth of large raindrops at lower levels.

observed by a C-band polarimetric radar mounted on the research vessel *Tan Kah Kee*, providing valuable dual-polarization measurements. In this study, we identify CCs based on Z_H and use multiple data, including CMA's TC database, ERA5 reanalysis data, and research vessel observations to investigate the microphysical properties of Choiwan's outer rainband.

Throughout the eight-hour observation period, both the TC and its outer rainband experienced notable changes, characterized by phases of strengthening and weakening. This eight-hour interval is divided into three stages: pre-mature, mature, and post-mature, mainly based on changes observed in the time-height distributions of polarimetric parameters. In general, the outer rainband CCs exhibit primarily small to mid-size drops across all three stages. Distinct microphysical characteristics are identified in each stage, as illustrated in a schematic diagram (Figure 4) and summarized below:

1. During the pre-mature stage, ice-phase processes are predominant, leading to the formation of graupels and the generation of large raindrops driven by the melting of ice particles. The DSDs at this stage are characterized by relatively higher diameters and lower number concentrations.
2. During the mature stage, both ice-phase and warm rain processes are simultaneously active. Ice-phase processes might lead to the rounded ice particles through strong riming process near the freezing level, and favor the formation of extremely large raindrops by melting. In contrast, warm rain processes play a key role in producing high concentrations of small raindrops below the freezing level. The majority of CCs near the convective system center consist of high concentrations of small raindrops, with a few peripheral CCs featured by extremely large drops.
3. During the post-mature stage, convection is less intense than in earlier stages, yet some level of intensification persists, supporting the continued dominance of ice-phase processes, resulting in the similarities in microphysical structures and DSDs between the post-mature and pre-mature stages. Different from the pre-mature stage, warm rain processes play a significant role in raindrop growth at lower levels in the post-mature stage.

In this study, the simultaneous activation of both ice-phase and warm rain processes during the mature stage in the outer rainband contrasts with the findings of D. Wu et al. (2018), where ice-phase processes predominated in an outer rainband over land. The active warm rain processes observed in Choiwan's outer rainband during the mature stage are likely closely linked to the oceanic environment. This environment might facilitate the condensation of water vapor through intense sea surface evaporation, further promoting warm rain processes (Feng et al., 2023).

Moreover, the possible generation of large quantities of sea spray through wave-breaking processes under TC conditions (Ma et al., 2020; Wang et al., 2001; Xu et al., 2023) may also enhance warm rain processes (Liu et al., 2022).

However, it is important to recognize that the empirical relationships used in this study introduce some uncertainty into the retrieved variables. Alternative empirical relationships (e.g., Wang et al., 2016; Zheng et al., 2021) are also tested, and while they produce different numerical values, the overall results remain consistent with our findings (Figure S9 in Supporting Information S1). Moreover, Choiwan represents only a single case, and its microphysical characteristics may not be broadly applicable to other TCs in the South China Sea, as each TC has unique characteristics influenced by various environmental factors. Additional field experiments on TCs in the South China Sea using ship-borne radars are essential. Comparative analysis of the similarities and discrepancies among different TC cases will provide a more comprehensive understanding of the microphysical characteristics of TCs in this region. Future research, potentially involving numerical simulations or other methodologies, is needed to further investigate the detailed microphysical processes and their roles in precipitation development.

Data Availability Statement

The CMA Tropical Cyclone Best Track Dataset used in this study can be accessed from the CMA Tropical Cyclone Data Center via https://tcdata.typhoon.org.cn/en/zjljsjj.html (Lu et al., 2021; Ying et al., 2014). The ERA5 reanalysis data are available at Copernicus Climate Change Service Climate Data Store (Hersbach et al., 2023). Research vessel data are available at Zenodo (Yang et al., 2024).

Acknowledgments

This study was supported by the Projects of Southern Marine Science and Engineering Guangdong Laboratory (Zhuhai) (Nos. SML2023SP209 and 311024001), the National Natural Science Foundation of China (No. 42475002), the Guangdong Basic and Applied Basic Research Foundation (2024A1515510005), and the Key Innovation Team of China Meteorological Administration (CMA2023ZD08). We acknowledge the high-performance computing support from School of Atmospheric Sciences of Sun Yat-sen University. We also acknowledge the KK2101 expedition team aboard the research vessel *Tan Kah Kee* for their invaluable in-situ observations in the South China Sea.

References

Boodoo, S., Hudak, D., Donaldson, N., & Leduc, M. (2010). Application of dual-polarization radar melting-layer detection algorithm. *Journal of Applied Meteorology and Climatology*, *49*(8), 1779–1793. https://doi.org/10.1175/2010JAMC2421.1

Bringi, V. N., Chandrasekar, V., Hubbert, J., Gorgucci, E., Randeu, W. L., & Schoenhuber, M. (2003). Raindrop size distribution in different climatic regimes from disdrometer and dual-polarized radar analysis. *Journal of the Atmospheric Sciences*, *60*(2), 354–365. https://doi.org/10.1175/1520-0469(2003)060<0354:RSDIDC>2.0.CO;2

Bringi, V. N., Huang, G.-J., Chandrasekar, V., & Gorgucci, E. (2002). A methodology for estimating the parameters of a gamma raindrop size distribution model from polarimetric radar data: Application to a squall-line event from the TRMM/Brazil campaign. *Journal of Atmospheric and Oceanic Technology*, *19*(5), 633–645. https://doi.org/10.1175/1520-0426(2002)019<0633:AMFETP>2.0.CO;2

Carey, L. D., & Rutledge, S. A. (2000). The relationship between precipitation and lightning in tropical Island convection: A C-band polarimetric radar study. *Monthly Weather Review*, *128*(8), 2687–2710. https://doi.org/10.1175/1520-0493(2000)128<2687:TRBPAL>2.0.CO;2

Chang, W.-Y., Lee, W.-C., & Liou, Y.-C. (2015). The kinematic and microphysical characteristics and associated precipitation efficiency of subtropical convection during SoWMEX/TiMREX. *Monthly Weather Review*, *143*(1), 317–340. https://doi.org/10.1175/MWR-D-14-00081.1

Chang, W.-Y., Wang, T.-C. C., & Lin, P.-L. (2009). Characteristics of the raindrop size distribution and drop shape relation in typhoon systems in the Western Pacific from the 2D video disdrometer and NCU C-band polarimetric radar. *Journal of Atmospheric and Oceanic Technology*, *26*(10), 1973–1993. https://doi.org/10.1175/2009JTECHA1236.1

Chen, G., Zhao, K., Zhang, G., Huang, H., Liu, S., Wen, L., et al. (2017). Improving polarimetric C-band radar rainfall estimation with two-dimensional video disdrometer observations in eastern China. *Journal of Hydrometeorology*, *18*(5), 1375–1391. https://doi.org/10.1175/JHM-D-16-0215.1

Cifelli, R., Petersen, W. A., Carey, L. D., Rutledge, S. A., & Da Silva Dias, M. A. F. (2002). Radar observations of the kinematic, microphysical, and precipitation characteristics of two MCSs in TRMM LBA. *Journal of Geophysical Research*, *107*(D20). https://doi.org/10.1029/2000JD000264

DeHart, J. C., & Bell, M. M. (2020). A comparison of the polarimetric radar characteristics of heavy rainfall from hurricanes Harvey (2017) and Florence (2018). *Journal of Geophysical Research: Atmospheres*, *125*(11), e2019JD032212. https://doi.org/10.1029/2019JD032212

Feng, L., Hu, S., Liu, X., Xiao, H., Pan, X., Xia, F., et al. (2020). Precipitation microphysical characteristics of typhoon Mangkhut in southern China using 2D video disdrometers. *Atmosphere*, *11*(9), 975. https://doi.org/10.3390/atmos11090975

Feng, L., Xiao, H., Liu, X., Hu, S., Li, H., Xiao, L., & Hao, X. (2023). Precipitation microphysical characteristics of typhoon Ewiniar (2018) before and after its final landfall over southern China. *Advances in Atmospheric Sciences*, *40*(6), 1005–1020. https://doi.org/10.1007/s00376-022-2135-x

Golestani, Y., Chandrasekar, V., & Bringi, V. N. (1989). Intercomparison of multiparameter radar measurements. In *Preprints, 24th conference on radar meteorology* (pp. 309–314). American Meteorological Society.

Gorgucci, E., Chandrasekar, V., Bringi, V. N., & Scarchilli, G. (2002). Estimation of raindrop size distribution parameters from polarimetric radar measurements. *Journal of the Atmospheric Sciences*, *59*(15), 2373–2384. https://doi.org/10.1175/1520-0469(2002)059<2373:EORSDP>2.0.CO;2

Gou, Y., Ma, Y., Chen, H., & Yin, J. (2018). Utilization of a C-band polarimetric radar for severe rainfall event analysis in complex Terrain over eastern China. *Remote Sensing*, *11*(1), 22. https://doi.org/10.3390/rs11010022

Haddad, Z. S., Durden, S. L., & Im, E. (1996). Parameterizing the raindrop size distribution. *Journal of Applied Meteorology*, *35*(1), 3–13. https://doi.org/10.1175/1520-0450(1996)035<0003:PTRSD>2.0.CO;2

Han, B., Du, Y., Wu, C., & Liu, X. (2021). Microphysical characteristics of the coexisting frontal and warm-sector heavy rainfall in South China. *Journal of Geophysical Research: Atmospheres*, *126*(21), e2021JD035446. https://doi.org/10.1029/2021JD035446

Hersbach, H., Bell, B., Berrisford, P., Biavati, G., Horányi, A., Muñoz Sabater, J., et al. (2023). ERA5 hourly data on single levels from 1940 to present (updated daily). *Copernicus Climate Change Service (C3S) Climate Data Store (CDS)*. [Dataset]. https://doi.org/10.24381/cds.adbb2d47

Hu, J., Rosenfeld, D., Ryzhkov, A., & Zhang, P. (2020). Synergetic use of the WSR-88D radars, GOES-R satellites, and lightning networks to study microphysical characteristics of hurricanes. *Journal of Applied Meteorology and Climatology*, *59*(6), 1051–1068. https://doi.org/10.1175/JAMC-D-19-0122.1

Janapati, J., Seela, B. K., Reddy, M. V., Reddy, K. K., Lin, P.-L., Rao, T. N., & Liu, C.-Y. (2017). A study on raindrop size distribution variability in before and after landfall precipitations of tropical cyclones observed over southern India. *Journal of Atmospheric and Solar-Terrestrial Physics*, *159*, 23–40. https://doi.org/10.1016/j.jastp.2017.04.011

Kou, L., Li, Y., Chu, Z., & Xu, F. (2018). C-Band dual-polarization Doppler weather radar data analysis and its application in quantitative precipitation estimation (in Chinese). *Journal of Tropical Meteorology*, *34*(4), 460–471. https://doi.org/10.16032/j.issn.1004-4965.2018.04.003

Kumar, A., Rao, T. N., Rao, N. R., & Radhakrishna, B. (2024). Unraveling the microphysical processes in convective cells during the passage of Nivar cyclone using X-band dual-polarization radar. *Atmospheric Research*, *309*, 107593. https://doi.org/10.1016/j.atmosres.2024.107593

Kumjian, M. R., & Prat, O. P. (2014). The impact of raindrop collisional processes on the polarimetric radar variables. *Journal of the Atmospheric Sciences*, *71*(8), 3052–3067. https://doi.org/10.1175/JAS-D-13-0357.1

Kumjian, M. R., Prat, O. P., Reimel, K. J., Van Lier-Walqui, M., & Morrison, H. C. (2022). Dual-polarization radar fingerprints of precipitation physics: A review. *Remote Sensing*, *14*(15), 3706. https://doi.org/10.3390/rs14153706

Li, H., Moisseev, D., & Von Lerber, A. (2018). How does riming affect dual-polarization radar observations and snowflake shape? *Journal of Geophysical Research: Atmospheres*, *123*(11), 6070–6081. https://doi.org/10.1029/2017JD028186

Li, H., Wan, Q., Peng, D., Liu, X., & Xiao, H. (2020). Multiscale analysis of a record-breaking heavy rainfall event in Guangdong, China. *Atmospheric Research*, *232*, 104703. https://doi.org/10.1016/j.atmosres.2019.104703

Li, Z., Wang, C., Li, C., Gao, Y., & Chen, D. (2014). Engineering calibration methods for differential reflectivity of dual polarization weather radar in simultaneous transmission and reception mode (in Chinese). *Meteorological Science and Technology*, *42*, 951–956. https://doi.org/10.19517/j.1671-6345.2014.06.001

Liu, F., Mao, F., Rosenfeld, D., Pan, Z., Zang, L., Zhu, Y., et al. (2022). Opposing comparable large effects of fine aerosols and coarse sea spray on marine warm clouds. *Communications Earth and Environment*, *3*(1), 232. https://doi.org/10.1038/s43247-022-00562-y

Liu, X., Wan, Q., Wang, H., Xiao, H., Zhang, Y., Zheng, T., & Feng, L. (2018). Raindrop size distribution parameters retrieved from Guangzhou S-band polarimetric radar observations. *Journal of Meteorological Research*, *32*(4), 571–583. https://doi.org/10.1007/s13351-018-7152-4

Lu, X., Yu, H., Ying, M., Zhao, B., Zhang, S., Lin, L., et al. (2021). Western North pacific tropical cyclone database created by the China meteorological administration. *Advances in Atmospheric Sciences*, *38*(4), 690–699. https://doi.org/10.1007/s00376-020-0211-7

Ma, H., Babanin, A. V., & Qiao, F. (2020). Field observations of sea spray under tropical cyclone Olwyn. *Ocean Dynamics*, *70*(11), 1439–1448. https://doi.org/10.1007/s10236-020-01408-x

Nzeukou, A., Sauvageot, H., Ochou, A. D., & Kebe, C. M. F. (2004). Raindrop size distribution and radar parameters at Cape Verde. *Journal of Applied Meteorology*, *43*(1), 90–105. https://doi.org/10.1175/1520-0450(2004)043<0090:RSDARP>2.0.CO;2

Okachi, H., Yamada, T. J., Baba, Y., & Kubo, T. (2020). Characteristics of rain and sea spray droplet size distribution at a marine tower. *Atmosphere*, *11*(11), 1210. https://doi.org/10.3390/atmos11111210

Radhakrishna, B. (2022). Raindrop size distribution (DSD) during the passage of tropical cyclone Nivar: Effect of measuring principle and wind on DSDs and retrieved rain integral and polarimetric parameters from impact and laser disdrometers. *Atmospheric Measurement Techniques*, *15*(22), 6705–6722. https://doi.org/10.5194/amt-15-6705-2022

Radhakrishna, B., & Narayana Rao, T. (2010). Differences in cyclonic raindrop size distribution from southwest to northeast monsoon season and from that of noncyclonic rain. *Journal of Geophysical Research: Atmospheres*, *115*(D16), 2009JD013355. https://doi.org/10.1029/2009JD013355

Seliga, T. A., & Bringi, V. N. (1976). Potential use of radar differential reflectivity measurements at orthogonal polarizations for measuring precipitation. *Journal of Applied Meteorology*, *15*(1), 69–76. https://doi.org/10.1175/1520-0450(1976)015<0069:PUORDR>2.0.CO;2

Seliga, T. A., & Bringi, V. N. (1978). Differential reflectivity and differential phase shift: Applications in radar meteorology. *Radio Science*, *13*(2), 271–275. https://doi.org/10.1029/RS013i002p00271

Skwira, G. D., Schroeder, J. L., & Peterson, R. E. (2005). Surface observations of landfalling hurricane rainbands. *Monthly Weather Review*, *133*(2), 454–465. https://doi.org/10.1175/MWR-2866.1

Subrahmanyam, K. V., & Baby, S. R. (2020). C-band Doppler weather radar observations during the passage of tropical cyclone 'Ockhi'. *Natural Hazards*, *104*(3), 2197–2211. https://doi.org/10.1007/s11069-020-04268-2

Tang, Q., Xiao, H., Guo, C., & Feng, L. (2014). Characteristics of the raindrop size distributions and their retrieved polarimetric radar parameters in northern and southern China. *Atmospheric Research*, *135–136*, 59–75. https://doi.org/10.1016/j.atmosres.2013.08.003

Testud, J., Le Bouar, E., Obligis, E., & Ali-Mehenni, M. (2000). The rain profiling algorithm applied to polarimetric weather radar. *Journal of Atmospheric and Oceanic Technology*, *17*(3), 332–356. https://doi.org/10.1175/1520-0426(2000)017<0332:TRPAAT>2.0.CO;2

Testud, J., Oury, S., Black, R. A., Amayenc, P., & Dou, X. (2001). The concept of "normalized" distribution to describe raindrop spectra: A tool for cloud physics and cloud remote sensing. *Journal of Applied Meteorology*, *40*(6), 1118–1140. https://doi.org/10.1175/1520-0450(2001)040<1118:TCONDT>2.0.CO;2

Tokay, A., Bashor, P. G., Habib, E., & Kasparis, T. (2008). Raindrop size distribution measurements in tropical cyclones. *Monthly Weather Review*, *136*(5), 1669–1685. https://doi.org/10.1175/2007MWR2122.1

Ulbrich, C. W. (1983). Natural variations in the analytical form of the raindrop size distribution. *Journal of Climate and Applied Meteorology*, *22*(10), 1764–1775. https://doi.org/10.1175/1520-0450(1983)022<1764:NVITAF>2.0.CO;2

Wang, H., Kong, F., Wu, N., Lan, H., & Yin, J. (2019). An investigation into microphysical structure of a squall line in South China observed with a polarimetric radar and a disdrometer. *Atmospheric Research*, *226*, 171–180. https://doi.org/10.1016/j.atmosres.2019.04.009

Wang, M., Zhao, K., Xue, M., Zhang, G., Liu, S., Wen, L., & Chen, G. (2016). Precipitation microphysics characteristics of a Typhoon Matmo (2014) rainband after landfall over eastern China based on polarimetric radar observations. *Journal of Geophysical Research: Atmospheres*, *121*(20). https://doi.org/10.1002/2016JD025307

Wang, Y., Kepert, J. D., & Holland, G. J. (2001). The effect of sea spray evaporation on tropical cyclone boundary layer structure and intensity. *Monthly Weather Review*, *129*(10), 2481–2500. https://doi.org/10.1175/1520-0493(2001)129<2481:TEOSSE>2.0.CO;2

Wen, L., Zhao, K., Chen, G., Wang, M., Zhou, B., Huang, H., et al. (2018). Drop size distribution characteristics of seven typhoons in China. *Journal of Geophysical Research: Atmospheres*, *123*(12), 6529–6548. https://doi.org/10.1029/2017JD027950

Willoughby, H. E., Marks, F. D., & Feinberg, R. J. (1984). Stationary and moving convective bands in hurricanes. *Journal of the Atmospheric Sciences*, *41*(22), 3189–3211. https://doi.org/10.1175/1520-0469(1984)041<3189:SAMCBI>2.0.CO;2

Wu, C., Liu, L., Wei, M., Xi, B., & Yu, M. (2018). Statistics-based optimization of the polarimetric radar hydrometeor classification algorithm and its application for a squall line in South China. *Advances in Atmospheric Sciences*, *35*(3), 296–316. https://doi.org/10.1007/s00376-017-6241-0

Wu, D., Zhao, K., Kumjian, M. R., Chen, X., Huang, H., Wang, M., et al. (2018). Kinematics and microphysics of convection in the outer rainband of typhoon Nida (2016) revealed by polarimetric radar. *Monthly Weather Review*, *146*(7), 2147–2159. https://doi.org/10.1175/MWR-D-17-0320.1

Wu, Z., Huang, Y., Zhang, Y., Zhang, L., Lei, H., & Zheng, H. (2021). Precipitation characteristics of typhoon Lekima (2019) at landfall revealed by joint observations from GPM satellite and S-band radar. *Atmospheric Research*, *260*, 105714. https://doi.org/10.1016/j.atmosres.2021.105714

Xu, X., Voermans, J. J., Zhang, W., Zhao, B., Qiao, F., Liu, Q., et al. (2023). Tropical cyclone modeling with the inclusion of wave-coupled processes: Sea spray and wave turbulence. *Geophysical Research Letters*, *50*(24), e2023GL106536. https://doi.org/10.1029/2023GL106536

Yang, S., Du, Y., Han, B., Wu, C., & Kong, H. (2024). Research vessel data. *Zenodo*. [Dataset]. https://doi.org/10.5281/zenodo.13627865

Ying, M., Zhang, W., Yu, H., Lu, X., Feng, J., Fan, Y., et al. (2014). An overview of the China meteorological administration tropical cyclone database. *Journal of Atmospheric and Oceanic Technology*, *31*(2), 287–301. https://doi.org/10.1175/JTECH-D-12-00119.1

Zhang, G., Vivekanandan, J., & Brandes, E. (2001). A method for estimating rain rate and drop size distribution from polarimetric radar measurements. *IEEE Transactions on Geoscience and Remote Sensing*, *39*(4), 830–841. https://doi.org/10.1109/36.917906

Zhang, G., Vivekanandan, J., Brandes, E. A., Meneghini, R., & Kozu, T. (2003). The shape–slope relation in observed gamma raindrop size distributions: Statistical error or useful information? *Journal of Atmospheric and Oceanic Technology*, *20*(8), 1106–1119. https://doi.org/10.1175/1520-0426(2003)020<1106:TSRIOG>2.0.CO;2

Zhang, Y., Zheng, H., Zhang, L., Huang, Y., Liu, X., & Wu, Z. (2021). Assessing the effect of riming on snow microphysics: The first observational study in east China. *Journal of Geophysical Research: Atmospheres*, *126*(7), e2020JD033763. https://doi.org/10.1029/2020JD033763

Zheng, H., Zhang, Y., Li, H., Wu, Z., Xie, Y., & Zhang, L. (2024). Raindrop deformation in turbulence. *Geophysical Research Letters*, *51*(9), e2024GL108627. https://doi.org/10.1029/2024GL108627

Zheng, H., Zhang, Y., Zhang, L., Lei, H., & Wu, Z. (2021). Precipitation microphysical processes in the inner rainband of tropical cyclone Kajiki (2019) over the South China sea revealed by polarimetric radar. *Advances in Atmospheric Sciences*, *38*(1), 65–80. https://doi.org/10.1007/s00376-020-0179-3